


Study of inertial electrostatic confinement fusion using a finite-volume scheme for the one-dimensional Vlasov equation

Jeffrey Black, Mitikorn Wood-Thanan , Aaron Maroni , and Erik Sánchez 
Department of Physics, Portland State University, Portland, Oregon 97201, USA

 (Received 3 September 2020; revised 4 November 2020; accepted 29 January 2021; published 22 February 2021)

While the majority of fusion energy research is focused on magnetic confinement, there have been several alternative confinement methods aimed at the development of smaller and less expensive reactors. A number of these alternative reactors are based on a spherically convergent beam of recirculating ions and include designs such as inertial electrostatic confinement (IEC), multigrid IEC, and the periodically oscillating plasma sphere concept. Here, a fully time-dependent GPU-based Vlasov solver was developed in order to study these spherically convergent devices. This code solves the Vlasov equation for a spherically symmetric system using a finite-volume method with a modified flux to account for electrode transparency. The solver accounts for secondary electron emission, interactions between the charged particles, and collisional effects such as ionization and charge exchange. This code was used to investigate a system similar to the ion-injected device described by Hirsch (see [R. L. Hirsch, *J. Appl. Phys.* **38**, 4522 (1967)]), who had reported a neutron production rate for deuterium-deuterium reactions in the range of 10^6 to 10^7 neutrons per second, which was attributed to the formation of a virtual electrode structure near the center of the chamber. Attempts to reproduce this experiment [B. J. Egle, Ph.D. thesis, 2010] yielded similar fusion rates, though the majority of the reactions were found not to occur near the center of the chamber. The results of this Vlasov solver, considering only beam-beam and beam-background fusion reactions, show that beam-background reactions would be dominant in such an ion-injected device. This result is consistent with work by Baxter and Stuart, who proposed a simplified steady-state Boltzmann model. However, the result of both models are inconsistent with the experimental results, which indicate a higher neutron production rate, and an inverse pressure scaling trend. It is shown that the higher experimental rates may be explained by beam-target fusion between the ion beam and deuterium embedded on the inner surface of the cathode.

DOI: [10.1103/PhysRevE.103.023212](https://doi.org/10.1103/PhysRevE.103.023212)

I. INTRODUCTION

An inertial electrostatic confinement (IEC) fusion device consists of a vacuum chamber containing one or more spherical electrode grids designed to accelerate ions toward the center of the device, creating a spherically convergent beam in which ions may be recirculated through the partially transparent grids. While many IEC experiments involve the use of cathode grids constructed of wire mesh, an interesting feature of the original Farnsworth-Hirsch configuration [1–3] was that the cathode grid was largely opaque, and ions were injected into the cathode region through small ports using six diametrically opposed ion guns. Any openings into the grid were held at a negative bias to permit the inward flow of ions while confining secondary electrons into the central region as much as possible. It was thought that this configuration could encourage the formation of one or more virtual electrodes in the central region, which could help facilitate ion trapping and increase the ion-ion fusion reaction rate. Hirsch's analysis of this system [2] assumed the injection of a monoenergetic ion beam in a spherically symmetric system, and predicted the development of a multiple virtual-electrode structure. Experimentally, Hirsch had reported a neutron production rate for such a device in the range of 10^6 to 10^7 neutrons per

second, and that this rate decreased with increasing pressure from 0.013 to 1.040 Pa (0.1 to 7.8 mTorr—for the purpose of making comparisons to previous work, non-SI units will be used hereafter).

Though IEC devices were originally investigated as potential fusion power sources, analysis such as that offered by Rider [4,5] and Nevins [6,7] point out the difficulties in obtaining net energy output from an IEC device. Particularly, since IEC relies on a non-Maxwellian distribution of particle energies, it is argued that the energy required to maintain this distribution over the timescale needed to obtain substantial fusion reactions would exceed the possible fusion power output. In addition to relaxation of the ion energy distribution, the angular momentum imparted to the ions during Coulomb scattering collisions will disturb the idealized spherical symmetry of the system.

Despite these critiques, there has been continued interest in IEC devices, particularly for their potential as low-cost neutron sources. There are a number of applications for neutron production via fusion reactions including: neutron activation analysis [8–10], medical isotope activation [11,12], neutron radiography [13,14], contraband and explosives detection [15–17], and space craft propulsion [18].

The development of a fast neutrons on-demand system could allow a user to generate neutrons and other high energy particles (^3He , ^4He , tritium and protons) using an inexpensive laboratory-based system and without the hazards of always active radioactive sources [19]. The appeal of using an IEC device for neutron generation is the possibility of using beam-beam reactions as a source regime (with greater than linear fusion rate scaling with current), instead of target based surface reactions. With further development of IEC systems and their variants, research into improving neutron production rates and applications can flourish, while the larger systems such as the international ITER project are developed for power applications.

Hirsch's fusion rate was unmatched by other IEC devices until recently, and was attributed to the organization of the discharge into a dense virtual electrode structure near the center of the chamber, as evident from collimated-neutron detection (suggesting beam-beam reactions as a primary source regime). However, more recent attempts [20] to recreate this experimental configuration have matched (and somewhat exceeded) the original results, but have called into question the source of fusion neutrons for such a device—there is evidence that beam background and beam target were the dominant reaction regimes in this case. Further, theoretical treatment by Baxter and Stuart [21], who proposed a steady-state Boltzmann model in linear geometry, predicted a similar neutron production rate (NPR) to Hirsch, attributed only to beam-background reactions. However, in this model the NPR pressure scaling curve only approaches Hirsch's data in a significantly higher pressure range.

In this study, a time-dependent numerical solver for the Vlasov-Poisson system in a spherically symmetric geometry was developed to analyze an ion-injected IEC device. Though a spherically symmetric system is highly idealized, it represents a “best-case” scenario for the conditions described by Farnsworth and Hirsch. In a real system, it is expected that ion-ion Coulomb scattering and imperfect focusing will impart an angular component to the ion velocity distribution. However, even in the context of spherical symmetry there are debated issues concerning the fusion source regime and the formation of virtual electrodes within the IEC discharge. The focus of this paper is to determine if a system operating under parameters similar to those described by Hirsch would be capable of trapping ions in a multiple virtual electrode structure, and to help elucidate the conflicting experimental and theoretical treatments of the fusion source regime in such a device. The simulations that were performed suggest that the NPR reported by Hirsch may arise primarily from beam-target reactions.

The Vlasov equation describes the time evolution of collisionless plasma:

$$\frac{\partial f_\alpha}{\partial t} + \vec{v} \cdot \frac{\partial f_\alpha}{\partial \vec{x}} + \vec{F} \cdot \frac{\partial f_\alpha}{\partial \vec{p}} = 0. \quad (1)$$

where $f_\alpha = f_\alpha(\vec{x}, \vec{p}, t)$ represents the phase-space density of particle species α (ions or electrons). The phase-space density represents the number of particles at a particular position \vec{x} , with momentum \vec{p} . (Here, \vec{v} is the time rate of change of \vec{x} , and \vec{F} is the time rate of change of \vec{p}). A self-consistent field, in

the electrostatic limit, is obtained by relating the phase-space density to the charge density [22]:

$$\rho(\vec{x}) = \sum_\alpha \int q_\alpha f_\alpha(\vec{x}, \vec{p}, t) d^3 p. \quad (2)$$

The associated electric potential then obeys the Poisson equation, with the space charge density (due to the free charges) acting as a source (in addition to any applied external potential):

$$\nabla^2 V = -\frac{\rho}{\epsilon_0}, \quad (3)$$

where V is the electrostatic scalar potential, ρ is the charge density, and ϵ_0 is the free space permittivity.

In this work, we consider the ions and electrons in the IEC discharge as weakly collisional, though some collisional effects with the background gas, including ionization, inelastic scattering, and charge exchange reactions are included by using the phase-space density to calculate the appropriate reaction rates. Previous studies have modeled IEC devices using particle-in-cell simulations [23–25], which use computational macroparticles to follow the characteristic curves of the Vlasov equation. The work described here uses a finite-volume scheme to directly solve the phase-space distribution on a finite mesh, using a conservation form of the Vlasov equation.

II. SIMULATION METHOD

For this study, we consider a phase space consisting of one radial spatial dimension and one radial momentum component (1D-1P). The spherical Vlasov-Poisson system is given by

$$\frac{\partial f_\alpha}{\partial t} + v_r \frac{\partial f_\alpha}{\partial r} + q_\alpha E_r \frac{\partial f_\alpha}{\partial p_r} = 0, \quad \frac{1}{r} \frac{\partial}{\partial r} \left(r^2 \frac{\partial \phi}{\partial r} \right) = -\frac{\rho}{\epsilon_0}. \quad (4)$$

In this case the phase-space density represents the number of particles within a spherical shell of radius r and width δr , with momentum in the range $(p_r, p_r + \delta p_r)$. The function f has units of number of particles per meter per momenta. Hereafter the radial subscripts will be assumed for velocity and momentum.

A. Finite-volume method (FVM) with effective electrode transparency

The numerical solver is implemented using the finite-volume method (FVM), where the phase-space density is represented on a rectangular mesh consisting of N_x spatial cells, with spacing Δx , and N_p momentum cells with spacing Δp . The average phase-space density within a mesh cell, at the k^{th} time step, is denoted $\bar{f}_{i,j}^k$, where i and j represent the position and momentum indices of a mesh cell, respectively. For a mesh cell with indices (i, j) , the radial position is given by

$$r_i = \left(i + \frac{1}{2}\right) \Delta x, \quad (5)$$

so that a radius of zero (the center of the chamber) is represented at the left edge of the domain, and the momentum is

given by

$$p_i = \left(j - \left\lfloor \frac{N_p}{2} \right\rfloor \right) \Delta p, \quad (6)$$

so that the zero of momentum is taken to be the cell with index $\lfloor N_p/2 \rfloor$. (It should be noted that Δx is the same for all species, but Δp is species dependent.) The simulation time is given by $t = k\Delta t$.

In the FVM, the Vlasov equation is integrated over the phase-space volume of a cell, and over one time step. This casts the equation into a conservation form where the change in the average phase-space density within one mesh cell is determined by the flux through the cell boundary averaged over one time step:

$$\bar{f}_{i,j}^{k+1} = \bar{f}_{i,j}^k - \frac{\Delta t}{\Delta x \Delta p} \sum_{m=0}^3 G_m. \quad (7)$$

In Eq. (7), the summation of G_m represents the time-averaged flux of phase-space density through the edges of a phase-space cell. The flux terms are approximated using the first-order Godunov flux functions [26]:

$$\begin{aligned} G_0 &= -\Delta p \begin{cases} v \bar{f}_{i-1,j}^k & v > 0 \\ v \bar{f}_{i,j}^k & v < 0, \end{cases} \\ G_1 &= \Delta x \begin{cases} F \bar{f}_{i,j}^k & F > 0 \\ F \bar{f}_{i,j+1}^k & F < 0, \end{cases} \\ G_2 &= \Delta p \begin{cases} v \bar{f}_{i,j}^k & v > 0 \\ v \bar{f}_{i+1,j}^k & v < 0, \end{cases} \\ G_3 &= -\Delta p \begin{cases} F \bar{f}_{i,j-1}^k & F > 0 \\ F \bar{f}_{i,j}^k & F < 0. \end{cases} \end{aligned} \quad (8)$$

Each of the four flux terms has two cases: flow into a mesh cell and flow out of a mesh cell. A unique feature of this solver is that for the velocity flow, the flux terms corresponding to an inward flow of particles are modified with an effective transparency coefficient which reduces the particle flux, representing particle loss to the electrode grids:

$$\begin{aligned} G_0 &= -\Delta p \begin{cases} k(p) v \bar{f}_{i-1,j}^k & v > 0 \\ v \bar{f}_{i,j}^k & v < 0, \end{cases} \\ G_2 &= \Delta p \begin{cases} v \bar{f}_{i,j}^k & v > 0 \\ k(p) v \bar{f}_{i+1,j}^k & v < 0. \end{cases} \end{aligned} \quad (9)$$

These transparency coefficients can be defined for each grid, and can be momentum dependent. This is useful when looking at systems like Hirsch's, in which ions are injected through portals and may not escape as easily.

B. Boundary conditions

The phase-space distribution is truncated at the momentum boundaries (the maximum momentum is made large enough that the particle density is negligible at this boundary), and at the boundary $r = r_{\max}$. At $r = 0$, a mirror symmetry boundary condition is employed so that $f(-r, p) = f(r, -p)$ at the

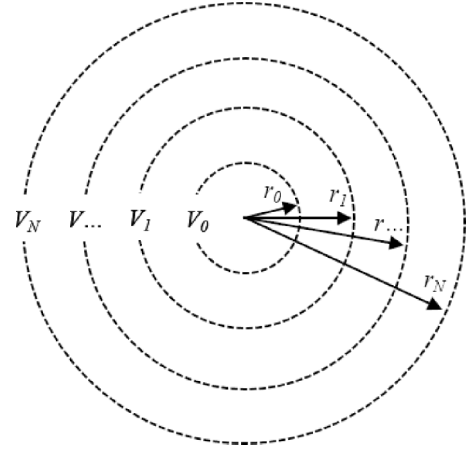


FIG. 1. A system of N spherically symmetric electrode grids. The simulation code takes the number of grids, as well as the radius and time-dependent potential of each grid, as user-defined parameters.

$i = 0$ mesh cell. At this boundary, as particles with negative momentum pass the center of the chamber, particles originating from the opposite side pass the center with a positive momentum at the same time. In the limit that $\Delta x \rightarrow 0$, the Coulomb force becomes large enough that no particle can pass through this symmetric boundary; this is the case of complete spherical convergence; since this is not attainable in a physical device, the symmetric boundary condition and the finite value of Δx together embody the effects of imperfect spherical focusing.

C. Electrostatic field solver

The code models a device consisting of any number of spherically symmetric electrode grids, held at a potential $V_n(t)$ (Fig. 1). When setting up a simulation, the user defines the number of electrodes, their radial locations (r_n), and the potential $V_n(t)$ at which each is held, which can be a user-supplied function of time. The largest electrode defines the outermost radius of the device (r_{\max}) and corresponds to the inner wall of a spherical vacuum chamber.

In the one-dimensional (1D) spherical system, the number density of particle species α is related to the 0th momentum moment $(\mu_0)_\alpha$ of its phase-space density by

$$n_\alpha(r) = \frac{\int f_\alpha(r, p) dp}{4\pi r^2} = \frac{(\mu_0)_\alpha}{4\pi r^2}, \quad (10)$$

giving a charge density of

$$\rho_\alpha(r) = \frac{q_\alpha (\mu_0)_\alpha}{4\pi r^2}. \quad (11)$$

The electric field within the device at a radius r is due to the effective charge of the closest electrode at r_n (such that $r_n < r$), as well as the free charge enclosed between r_n and r (the electrodes are assumed to shield any other enclosed charge). Letting Q_n , V_n , and r_n represent the effective charge, voltage, and radius of the n^{th} electrode (numbered in order of increasing radius), the effective charge for the n^{th} electrode

can be calculated from Gauss's law:

$$Q_n = \left[(V_n - V_{n+1}) + \int_{r_n}^{r_{n+1}} \frac{q_{\text{enc}}(r) dr}{4\pi\epsilon_0 r^2} \right] 4\pi\epsilon_0 \left(\frac{1}{r_n} - \frac{1}{r_{n+1}} \right)^{-1}, \quad (12)$$

where $q_{\text{enc}}(r)$ represents the free charge enclosed between r_n (the nearest electrode with radius less than r) and r :

$$q_{\text{enc}}(r) = \sum_{\alpha} \int_{r_n}^r \rho_{\alpha}(r') 4\pi r'^2 dr' = \sum_{\alpha} \int_{r_n}^r q_{\alpha}(\mu_0)_{\alpha} dr'. \quad (13)$$

In the discrete phase space, the 0th momentum moment is calculated as

$$(\mu_0)_{\alpha} = \sum_j (f_{i,j} \Delta p)_{\alpha} \Delta x, \quad (14)$$

and the integrals that appear in Eqs. (12) and (13) are calculated using a trapezoid rule. Once Q_n is known for all the electrodes, and q_{enc} is calculated for all spatial cells, the total electric field at the i^{th} spatial cell (between n and $n+1$) is directly calculated using Gauss's law:

$$E(r_i) = \frac{1}{4\pi\epsilon_0 r_i^2} (q_{\text{enc}}(r_i) + Q_n), \quad (15)$$

which satisfies the Poisson equation in spherical coordinates. In addition to the grid parameters, the user can also define the particle injection in terms of an injection current and the radius of a spherical injection surface.

D. Calculating the simulated neutron production rate and atomic processes

Once the phase-space distribution function, $f(r, p)$, is known at a time t , it can be integrated to determine the fusion rate. In general, to calculate the fusion rate density (reactions per volume per second) for collisions between two particle species (labeled 1 and 2), the number density (as a momentum distribution) for each species can be integrated as follows:

$$R_{\text{fusion}} = \iint \sigma(E_{\text{relative}}) |\vec{v}_1 - \vec{v}_2| n_1(\vec{p}_1) n_2(\vec{p}_2) d^3 p_1 d^3 p_2. \quad (16)$$

The factor $\sigma(E_{\text{relative}}) |\vec{v}_1 - \vec{v}_2|$ contains the relative velocity between the particle species and the fusion cross section which depends on the relative energy between the two species within a infinitesimal volume of phase space. This value will subsequently be abbreviated ($\sigma|v|$).

To calculate the NPR, two reaction regimes are considered: beam-beam reactions (between energetic particles, either ions or fast neutrals) and beam-background reactions (between the energetic particles and the background gas). In the 1D-1P spherical system, there is only one momentum component, and from Eq. (10) it can be seen that the momentum distribution of the number density is given by

$$n(r, p) = \frac{f(r, p)}{4\pi r^2}. \quad (17)$$

Using this expression in Eq. (16) for beam-beam reactions gives

$$R_{\text{beam}}(r) = \iint \frac{f_1(r, p) f_2(r, p)}{(4\pi r^2)^2} (\sigma_{DD} |v|) dp_1 dp_2. \quad (18)$$

(For same-species interactions, the double integral over momentum space is performed without double counting.) In this study, we are looking only at the neutron production rate, so in this context σ_{DD} refers only to the cross section for the $D(d, n)^3\text{He}$ reaction channel. These cross sections were evaluated using the parametrization described by Bosch and Hale [27]. For beam-background reactions, the momentum distribution for the background gas is considered to be a Dirac delta distribution, so Eq. (16) simplifies to:

$$R_{bg}(r) = n_0 \int \frac{f(r, p)}{(4\pi r^2)} (\sigma|v|) dp. \quad (19)$$

In both cases, the total neutron production rate is obtained by integrating the reaction rate density over the entire spherical volume:

$$NPR = \int (R_{bg}(r) + R_{\text{beam}}(r)) (4\pi r^2) dr. \quad (20)$$

In addition to the fusion rate discussed above, atomic processes between the charged particles (electrons and deuterons) and the neutral background gas are considered, these include: electron-impact ionization, ion-impact ionization, electron-impact excitation, ion-impact excitation, and charge-transfer (CX). The background gas is modeled as atomic deuterium with a negligible momentum distribution, and a uniform density n_0 throughout the volume. These reaction rates are evaluated in a similar manner to the beam-background fusion reactions [Eq. (19)], but with the appropriate cross section for the atomic process. The cross sections used for these charged particle neutral interactions are implementations of the fitting curves of Janev [28].

Energy interpolation

Ionization and excitation collisions between charged particles and neutrals result in small energy losses for the charged species of just a few eV. This small loss of energy is, in most cases, beyond the resolution of the momentum cell spacing (this is compounded by the nonlinear spacing in terms of energy). However, these energy losses should still be accounted for in order to determine overall device efficiency. If some fraction of the phase-space density, Δf , of a charged species is to be scattered to a lower energy due to neutral collisions, care should be taken to make sure that neither too little nor too much energy is lost in the simulation due to the limited resolution in momentum space.

In order to do this, an interpolation scheme based on conservation of energy and particle number was implemented. Consider two adjacent momentum cells, with indices j and j' , where j' represents the next lowest energy cell. Let $f_{i,j}$ and $f_{i,j'}$ be the densities before the collision, and let $f'_{i,j}$ and $f'_{i,j'}$ be the densities after the collision. The total particle number between the two cells is conserved:

$$\begin{aligned} f_{i,j} \Delta x \Delta p + f_{i,j'} \Delta x \Delta p &= f'_{i,j} \Delta x \Delta p + f'_{i,j'} \Delta x \Delta p \\ \Rightarrow (f_{i,j} - f'_{i,j}) &= -(f_{i,j'} - f'_{i,j'}) \\ \Rightarrow \Delta f_{i,j} &= \Delta f_{i,j'}. \end{aligned} \quad (21)$$

In addition, the change in the integrated energy over two adjacent momentum cells should equal ΔU , which represent

the total energy lost due to a particular collisional process within a cell over one time step:

$$\frac{p_j^2}{2m}(f_{i,j}\Delta x\Delta p) + p_{j'}^2 2m(f_{i,j'}\Delta x\Delta p) = \Delta U. \quad (22)$$

Using expression (6), and defining the relative momentum index $j_r = j - \lfloor N_p/2 \rfloor$, Eq. (22) becomes

$$\frac{\Delta x \Delta p^3}{2m} [(j_r)^2 \Delta f_{i,j} - (j_r \pm 1)^2 \Delta f_{i,j}] = \Delta U. \quad (23)$$

Using Eq. (23) to solve for $\Delta f_{i,j}$ gives the interpolation scheme:

$$\Delta f_{i,j} = \frac{2m\Delta U/\Delta x\Delta p^3}{[j_r^2 - (j_r \pm 1)^2]}. \quad (24)$$

[Here, $(j_r \pm 1)$ represents the nearest momentum cell with lower energy.]

E. Secondary electrons and backscattered particles

The role of secondary electron emission from the inner surface of the cathode electrode in the creation of a virtual cathode was discussed by Farnsworth [2]. A simple model of secondary electron emission and ion backscattering was included in the FVM Vlasov code in order to study the possible effects of these processes on the IEC discharge, fusion rate, and device efficiency. In each case, the incident particles are assumed to impact the grid structure at normal incidence. Due to the grid transparency, only a fraction of the incident flux is considered to have undergone a collision with the grid's surface. To calculate the fraction of incident particles giving rise to secondary electron emission (SEE), a modified form of Eq. (9) is used:

$$G_0 = -\Delta p \begin{cases} [k(p) - 1] v \bar{f}_{i-1,j}^k & v > 0 \\ v \bar{f}_{i,j}^k & v < 0, \end{cases} \quad (25)$$

$$G_2 = \Delta p \begin{cases} v \bar{f}_{i,j}^k & v > 0 \\ [k(p) - 1] v \bar{f}_{i+1,j}^k & v < 0. \end{cases}$$

where the coefficient $[k(p) - 1]$ determines the fraction of incidence particle flux lost to the grid. For electron-impact, the probabilistic model described by Pivi and Furman [29] was used to determine the SE yield and the energy of the secondary particles. The secondary electron emission is broken into three components: backscattered, rediffused, and true secondary electrons. For each momentum value represented on the finite grid, the yield ($N_{\text{emitted}}/N_{\text{incident}}$) and the average fraction of the incident energy ($E_{\text{emitted}}/E_{\text{incident}}$) of the emitted particles are evaluated for each component and stored as a look-up table. During the update step of the Vlasov simulation, the lost flux to the grid is evaluated for each momentum cell, and this value is multiplied by the appropriate SEE yield coefficient to determine the scattered flux. The scattered flux is added to back to the momentum cell corresponding to the scattered energy and opposite direction.

The secondary emission due to ion impact is considered to be proportional to the electronic stopping power (S_e) of the incident ions [30,31]. The electronic stopping power is determined for the relevant range of energies using the program

SRIM (Stopping and Range of Ions in Matter [32,33]), and the resulting curve is multiplied by the constant $\Lambda = 0.07442$ Å/eV. This constant was determined using a weighted average of the values compiled in Table III in Ref. [31] for Fe, Ni, and Cr, with the weights 0.74, 0.18 and 0.08 reflecting the composition of stainless steel. The ion-induced secondary electrons were assumed to have negligible energy in the Vlasov simulation (the peaks of the secondary spectrum are assumed to be only a few eV [34]). The yield of backscattered ions and their average energies were computed using TRIM (Transport of Ions in Matter [32]) for ions at normal incidence on stainless steel over the possible range of incident energies. Interpolation between the tabulated values obtained from SRIM/TRIM was performed within the Vlasov simulation to obtain the approximate coefficients needed for the ion-induced secondary electron and backscattered ion yields.

F. Implementation

For the finite volume scheme to be numerically stable, an adaptive time step is used. The allowed time step for an individual species is

$$\Delta t = \frac{1}{2} \min \left(\frac{\Delta p}{|qE_{\text{max}}|}, \frac{\Delta x}{|v_{\text{max}}|} \right), \quad (26)$$

and the simulation is advanced using the smallest Δt among all species. (Time steps are typically on the order of $\Delta t \approx 1 \times 10^{-14}$ s for the runs performed on this study). The code was written with C++/CUDA, as Eqs. (7) and (8) can be computed independently for each phase-space cell, which lends itself well to parallelization. Several of the auxiliary equations described above rely on taking momentum moments of the phase-space distributions; in this case, the moments can be computed using parallel reduction algorithms, which greatly speeds computation times. For the present study, the resolution of the phase-space mesh used was 1024×1024 cells, and the momentum space was truncated to the momentum of a particle accelerated by $10\times$ the cathode potential (for example, a simulation with a cathode potential of -100 kV has a maximum represented momentum corresponding to a particle accelerated to 1 MeV).

To verify convergence of the neutron production rate, the solver was run multiple times with the same physical parameters, but at various mesh resolutions. The results of this convergence test are shown in Fig. 2. For each trial, the simulation was run until an approximately steady-state NPR was achieved (typically after 5×10^6 iterations), while the NPR was logged every 1×10^4 iterations (500 data points total). Due to small variations about the steady-state value, an average of the last 50 data points is used as the reported NPR. The geometry used in these tests matches that described in the following section.

III. SIMULATION RESULTS

A. Simulation of Hirsch's IEC device

In an attempt to simulate the six ion gun device described by Hirsch, the simulation was set up with two electrodes: a solid, grounded anode of radius $r_A = 8.9$ cm, and a semi-transparent cathode of radius $r_C = 5.7$ cm with a potential V_C

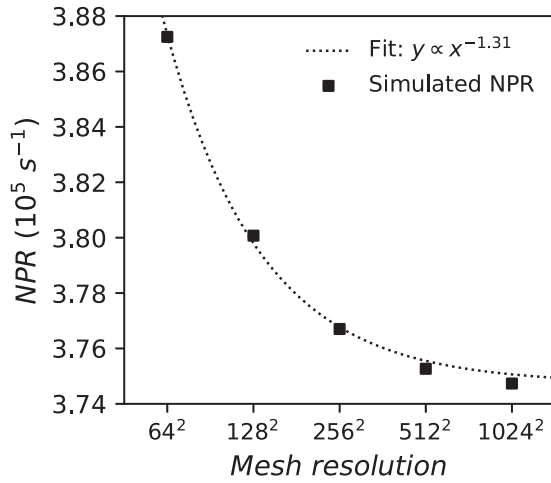


FIG. 2. Convergence testing for the neutron production rate at $n_0 = 1.0$ mTorr, $V_C = -110$ kV, with an ion injection current of 10 mA.

applied by a power supply with an output limited to 10 kW. An ion current of $I_i = 10$ mA was injected at the inner anode surface. The geometry of this configuration is shown in Fig. 3. Note that instead of six converging beams, the simulation assumes a radially symmetric ion injection distributed over a spherical surface, with the transparency coefficient of the cathode emulating the admittance of ions through an acceptance port, and their subsequent trapping within the largely opaque cathode structure. This transparency coefficient was defined for the ions as

$$k(p) = \begin{cases} 0.05 & p > 0 \\ 0.95 & p < 0, \end{cases} \quad (27)$$

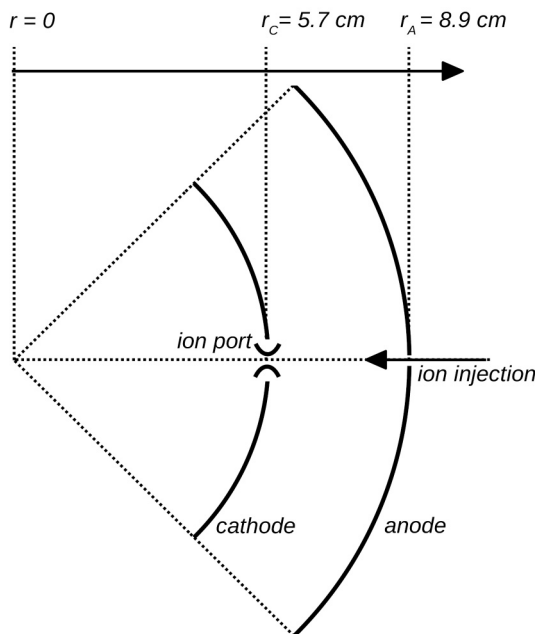


FIG. 3. Schematic representation of the geometry used in simulating the ion-injected IEC device.

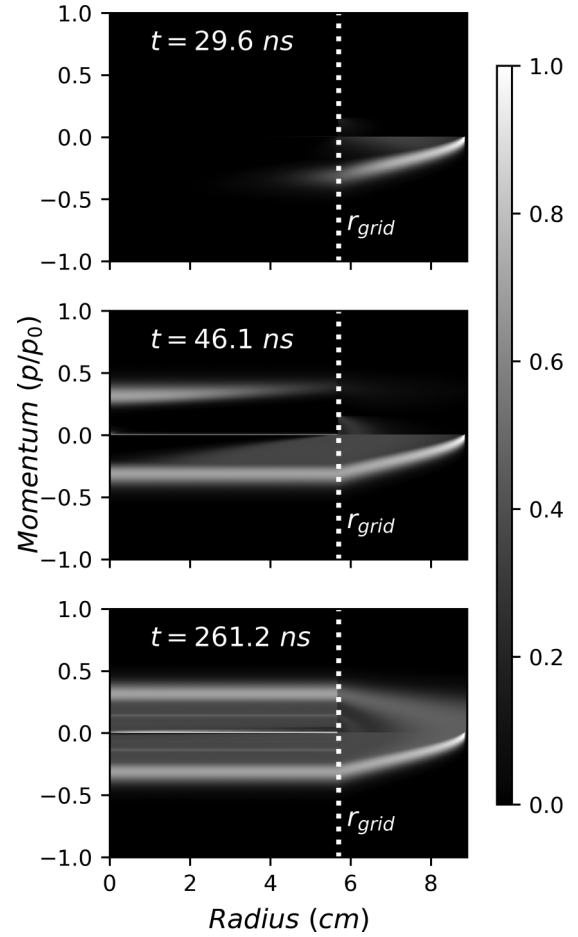


FIG. 4. Representative snapshots of the phase-space density for ions as determined using the time-dependent Vlasov model. (Here, $n_0 = 1.0$ mTorr, $V_C = -110$ kV, $I_{ion} = 10$ mA.)

this momentum dependence makes it so the majority of injected ions are admitted through the cathode (due to the acceptance ports) on their first pass, while being trapped within the inner cathode region on subsequent transits through the chamber. For the electrons, the transparency was set to $k(p) = 0.05$, representing confinement of the electrons to the inner region of the cathode, as was the case described by Farnsworth [3] and Hirsch [2].

Representative samples of the simulation results for the ion species are shown in Fig. 4. The cold beam of ions is injected near $r_{max} = 8.9$ cm, and accelerated by the cathode grid at $r_{grid} = 5.7$ cm. As the ion density reaches the chamber's center, ions injected from the other side reach the center at the same time with opposite momentum, resulting in the mirror-symmetric boundary near $r = 0$. Note that as ions with positive momentum encounter the inner side of the cathode grid, only a fraction of them pass due to the transparency defined in Eq. (27).

For the first set of simulation runs, the solver was configured to include the effects of space charge, charge exchange, and ion/electron impact ionization and excitation (secondary electrons and backscattered ions were omitted). Each run used an injection current of $I = 10$ mA; and the background pressure was swept from 0.1 to 60 mTorr; this sweep was repeated

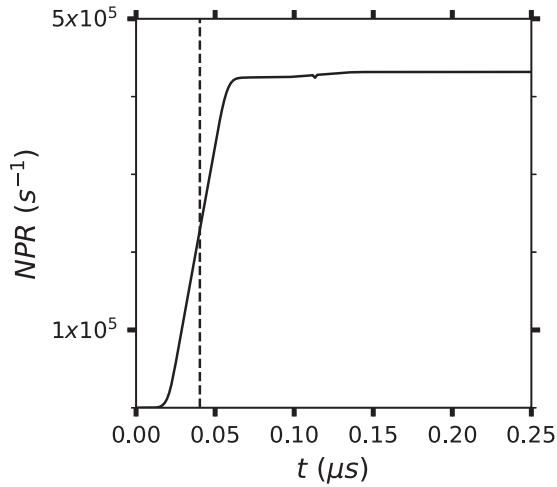


FIG. 5. Simulated neutron production rate over time (0.1 mTorr, $V_C = -110$ kV). The vertical dashed line represents the time it takes an ion starting from rest at the outer edge of the chamber to reach the center, as determined semi-analytically.

for cathode potentials of -50 , -70 , -90 , and -110 kV. (These parameters were chosen to cover the experimental values used by Hirsch.) For each trial, the simulation was run until an approximately steady-state NPR was achieved, as shown in Fig. 5. The collected results from this set of pressure sweeps are shown in Fig. 6.

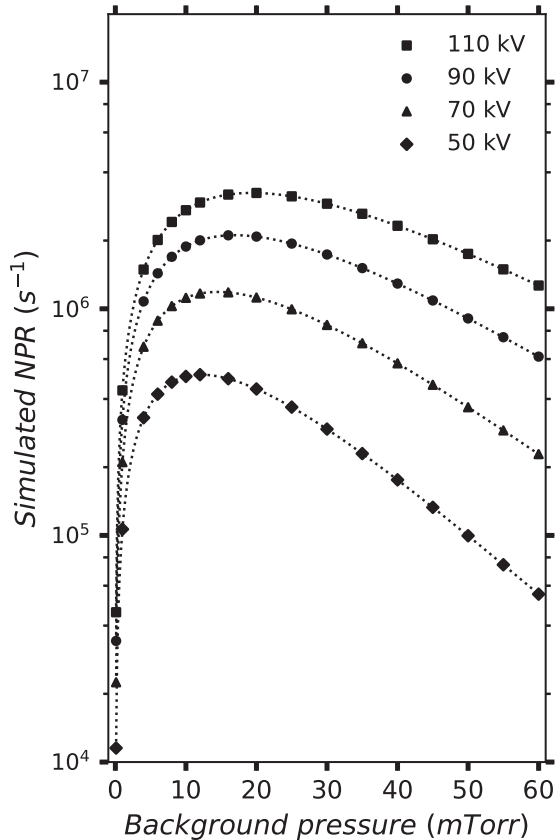


FIG. 6. The simulated NPR pressure scaling for a Hirsch-like device with pressure, for several cathode voltages.

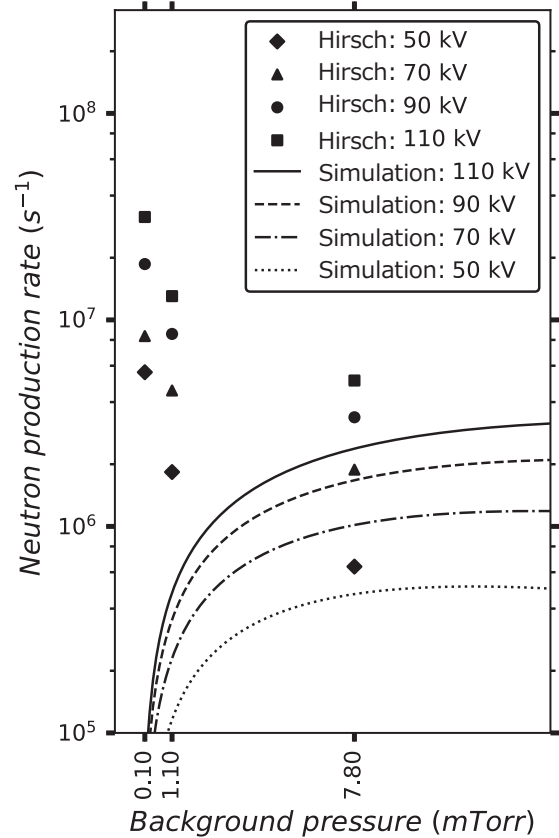


FIG. 7. The simulated NPR compared to Hirsch's results. Note that the pressure scaling trend is inverted in the experimental pressure range.

It was found that the NPR initially increases rapidly with pressure, consistent with ion-background reactions being the dominant source of fusion reactions. The NPR reaches a maximum value, after which loss mechanisms such as charge transfer begin to reduce the possible fusion rate. Plotting these results alongside the original data published by Hirsch

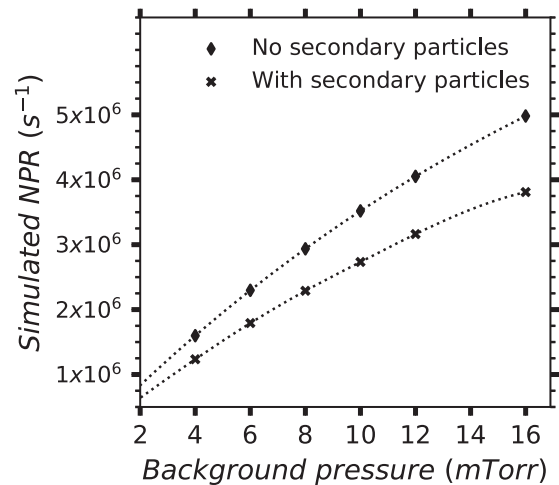


FIG. 8. The effects of secondary electron emission and backscattered particles on the fusion rate (0.1 mTorr, $V_C = -110$ kV).

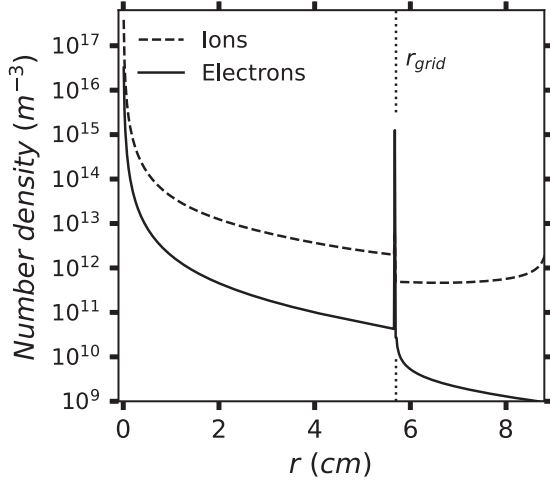


FIG. 9. The radial distribution of the particle number density (0.1 mTorr, $V_C = -110$ kV). The spike of electron density at the electrode grid is due to secondary electron emission.

(Fig. 7), it can be seen that the time-dependent Vlasov simulation shows a lower NPR and an inverse pressure scaling trend compared to the experiment results (though at 7.8 mTorr of background pressure the simulation does begin to approach the experimental results).

B. Effects of secondary electron emission

One aspect this simulation was aimed at investigating was the formation of multiple potential wells near the center of the cathode, which could be enhanced by secondary electron emission from the inner surface of the cathode grid, and the confinement of electrons to the inner cathode area.

However, with all other parameters being the same, the inclusion of secondary electrons and backscattered particles did not cause the NPR to vary much, making it less in some cases, and primarily caused the power supply model to reach its current limit at pressures above 16 mTorr. A comparison of the same pressure sweep at -110 kV with and without secondary particles is shown in Fig. 8. Steady-state snapshots of the particle and reaction rate densities are shown in Figs. 9 and 10, respectively. These snapshots were taken from a single run but are qualitatively similar to the profiles taken from other points in the pressure sweep. The particle density profile (Fig. 9) shows a sharp increase of ion density toward the center of the device and an overall higher density of ions throughout the inner region of the cathode. While this does give rise to an increase in electric potential toward the center of the device; no multiple virtual electrode structures were seen in any of the simulation runs performed. The simulated reaction rate is due to two contributions: ion-ion and ion-background fusion (including energetic neutrals created through charge exchange). The radial distribution of the reaction rate densities for both (Fig. 10) shows that ion-background reactions are the primary contributor to the overall fusion rate, which is consistent with estimates by Thorson [35].

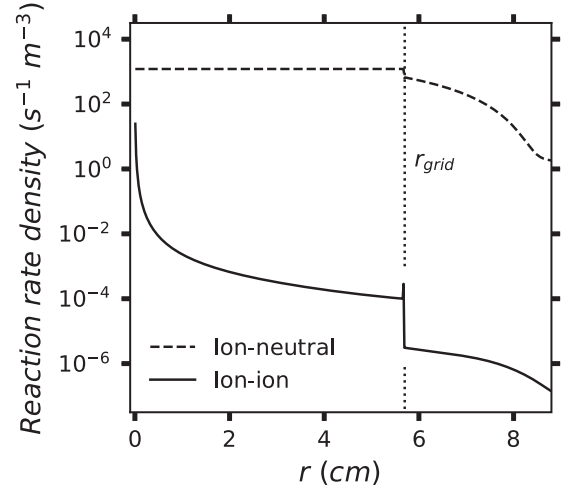


FIG. 10. Neutron production rate density, radial distribution (0.1 mTorr, $V_C = -110$ kV). The radius of the cathode grid is indicated by the vertical dashed line.

IV. DISCUSSION

A. Comparison with a previous steady-state model

A method for solving the steady-state Boltzmann equation applied to an IEC-like system was previously presented by Baxter and Stuart [21], who had reached similar results to what is reported here. Their model was based on the idea that a beam of ions interacting with a cold background of neutral particles could explain Hirsch's results. It was assumed that the ions would start at rest, and would undergo constant acceleration from anode to cathode, before drifting through the inner cathode region which is devoid of electric fields (space charge effects were neglected in this model). Ions that made it across the inner cathode region were lost to the inner surface of the cathode. Along the entire path, ions could undergo charge exchange with the background gas (resulting in the formation of fast neutral particles). Both the ions and the fast neutrals could undergo ionization, creating a spatially distributed ion source, as well as fusion reactions with the background gas. To validate the time-dependent Vlasov model described in the current work, the simulated NPR was compared to that predicted by this steady-state model.

To match the assumptions made in Baxter and Stuart's work, the following modifications were made to the time-dependent Vlasov model: the radial electric field was replaced with a constant electric field of magnitude $E_0 = V_C/(5 \text{ cm})$, the effects of space charge were removed, and the electron density function was omitted. Ion-neutral ionization and charge exchange effects were included. The simulation was set up with two electrodes: a solid, grounded anode of radius $r_A = 10.7 \text{ cm}$, and a cathode of radius $r_C = 5.7 \text{ cm}$. The cathode potential was set to $V_C = -100 \text{ kV}$. The cathode only permitted the flow of ions in one direction, this was accomplished by defining the transparency coefficient as

$$k(p) = \begin{cases} 0.0 & p > 0 \\ 1.0 & p < 0. \end{cases} \quad (28)$$

These parameters cause the time-dependent simulation to behave as a 1D linear system in slab geometry, with an ac-

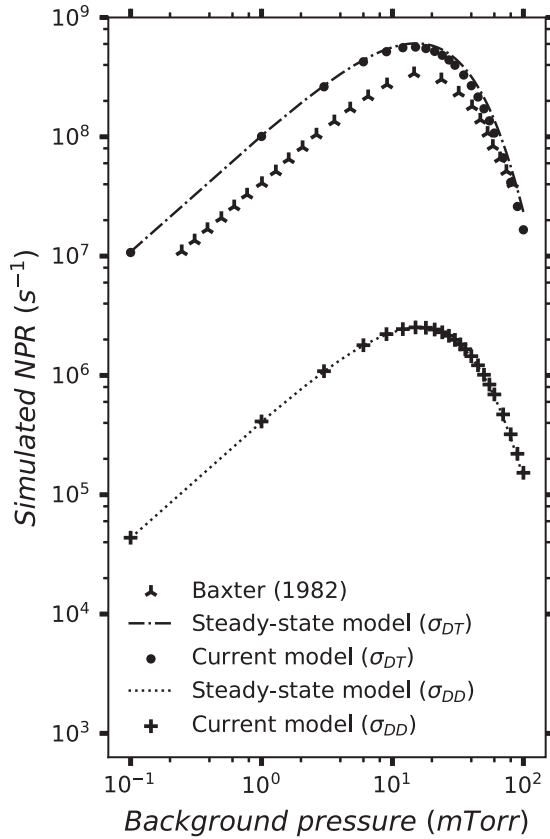


FIG. 11. Comparison of the time-dependent FVM Vlasov code to the steady-state model of Baxter and Stuart.

celeration region 5.0-cm long, and a field-free drift region 11.4 cm long (before an ion would collide with the inner cathode wall); this is the same system considered by Baxter and Stuart. The value of the background gas pressure, n_0 , was swept over the range 0.1–100 mTorr, and the neutron production rate was allowed to reach an equilibrium value which was recorded for each trial.

It should be mentioned that Baxter and Stuart's work was reproduced for this paper by numerically integrating Eq. (11) of their paper (see the Appendix for details). We believe that the modified numerical scheme used for this reproduction and the use of the fusion cross section parametrization described in Ref. [27] provides a more accurate result than that originally published in Ref. [21] and puts the two models into good agreement. This pressure sweep was performed using both the steady-state and time-dependent models, using both the DD (Deuterium-Deuterium) and DT (Deuterium-Tritium) cross sections. Both models give nearly identical results, which are shown Fig. 11.

B. The role of surface fusion

The time-dependent Vlasov model presented here predicts that beam-background fusion would be the primary source of neutrons in an ion-injected IEC device like that described by Farnsworth and Hirsch; the inclusion of secondary electrons and backscattered particles into the model does not lead to a substantially different outcome. While both the time-

dependent Vlasov model the steady-state model of Baxter and Stuart agree with each other (in the limiting case that such a comparison is applicable), both models fail to predict the NPR of Hirsch's experimental data and the observed pressure scaling relationship.

A possible explanation for this discrepancy is the role of embedded deuterium fusion, which is not an effect included in the Vlasov simulation. As ions pass through the cathode region, they collide with the inner wall of the cathode grid and implant into the metal surface acting as a target for the ion beam. Experimental evidence for this beam-target reaction being a primary fusion source in a six-ion gun device similar to Hirsch's (University of Wisconsin's SIGFE device) is discussed in Ref. [20]. The following calculation was used to obtain a rough estimate of the fusion rate due to embedded deuterium at -110 kV and 10 mA of ion current: The beam is considered monoenergetic, with a fusion rate per volume between the beam and the embedded target given by

$$dR_{\text{fusion}} = \frac{1}{2} n_{\text{target}} n_{\text{beam}} \langle \sigma(E) \rangle dV, \quad (29)$$

where dV is an infinitesimal volume over which the reactions occur. Assuming the ion beam has a uniform density over an incident surface area A , the volume element dV is given by $dV = A dx$, and the number density of the beam can be expressed as

$$|\vec{J}| = \frac{|\vec{I}|}{A}, \quad |\rho \vec{v}| = \frac{|\vec{I}|}{A}, \quad |en\vec{v}| = \frac{|\vec{I}|}{A}, \quad n_{\text{beam}} = \frac{|\vec{I}|}{evA}. \quad (30)$$

Inserting the expression for the beam density and the volume element into Eq. 29 gives the following expression for the infinitesimal fusion rate:

$$dR_{\text{fusion}} = \frac{1}{2} n_{\text{target}} \frac{I}{e} \sigma(E(x)) dx. \quad (31)$$

Due to energy loss via scattering of the incident ions within the target material, the fusion cross section becomes a function of depth, which is integrated over the ion range, d , to obtain the total fusion rate:

$$R_{\text{fusion}} = \frac{1}{2} n_{\text{target}} \frac{I}{e} \int_0^d \sigma(E(x)) dx. \quad (32)$$

This integral can be evaluated using the total stopping power, $S_t(x)$, as a function of depth:

$$E(x) = E_0 - \int_0^x S_t(x) dx, \quad (33)$$

where E_0 is the incident energy of the particles impinging on the metal surface. This gives the total fusion rate for the beam-target reaction:

$$R_{\text{fusion}} = \frac{1}{2} n_{\text{target}} \frac{I}{e} \int_0^d \underbrace{\sigma \left[E_0 - \int_0^x S_t(x) dx \right]}_{F(E_0)} dx, \quad (34)$$

$$R_{\text{fusion}} = \frac{1}{2} n_{\text{target}} \frac{I}{e} F(E_0).$$

The integral factor, $F(E_0)$, which depends only on the energy of the incident particles and the target material, was numerically integrated. To do so, TRIM was used to calculate the

total ion stopping power, $S_i(x)$, for 110 keV deuterium ions at normal incidence on stainless steel, as a function of depth; as before, the parametrization given in Ref. [27] was used to evaluate the DD cross section. Once $F(E_0)$ is determined, the fusion rate is proportional to the incident current (assumed to be 10 mA to match Hirsch's data), and n_{target} , the saturation density of embedded deuterium.

The effective saturation density is dependent on both temperature and previous damage to the target material [36,37]; since these are unknown in Farnsworth and Hirsch's experiments, an estimated density of $2 \times 10^{21} \text{ cm}^{-3}$ was assumed (this estimated value is chosen based on previous measurements [38–40]). These calculations give an embedded deuterium fusion rate of around $2.5 \times 10^7 \text{ N/s}$ which is nearly the value reported by Hirsch at the lowest pressure of 0.1 mTorr. This suggests that embedded deuterium fusion may explain the discrepancy between the kinetic model presented in this work, and the experimental results reported by Hirsch.

V. CONCLUSION

In this work, a time-dependent Vlasov solver was implemented using the finite volume method, and applied to an IEC device similar to that described by Hirsch in 1968. When considering only fusion reactions between the energetic particles and themselves or the background gas (neglecting embedded target fusion), it was found that the fusion rate of such a device, even with the inclusion of secondary electron emission and strong confinement of electrons, is consistent with beam-background fusion as a primary source. While these results are consistent with the steady-state model of Baxter and Stuart, they are inconsistent with the experimental results of Hirsch, who found an inverse pressure scaling trend. It is suggested that these experimental results may primarily be due to beam-target fusion between the ion beam and deuterium embedded on the inner surface of the cathode. This result is supported by experimental findings from another ion-injected device [20], as well as other IEC devices [39,41].

Farnsworth and Hirsch's design aimed to create a multiple virtual electrode structure within the inner radius of the cathode which would allow for the acceleration and recirculation of ions. With the parameters used in these simulation runs, no such multiple virtual electrode formation was noted, and there was little to no ion recirculation due to the transparency parameters chosen for the grid. However, with the 10-mA ion current used, space-charge effects were not dominant, so further work should be done simulating the operation of such a device at much higher ion injection currents where such effects can play a larger role in the discharge characteristics.

VI. FUTURE WORK

A primary reason this code was written was to study the efficiency of RF-modulated and high current IEC systems. A pulsed system may be able to take advantage of transient increases in the fusion rate efficiency; such modes of operation were suggested by Farnsworth [1], as well as Barnes and Nebel [42,43]. To understand the efficiency of a device with RF modulation, the Vlasov code should be coupled to an accurate model for the external power supply circuits, as

the discharge can couple to a multiple power supply system in a complicated way. A high-efficiency IEC device would require better ion confinement, lower background pressures and higher injection currents in order to leave the regime where beam-target and beam-background reactions are dominant. Under these conditions space charge effects are more appreciable (which has been seen in the Vlasov simulation at higher currents) giving a possibility for self-organization of the discharge under the influence of a pulsed external voltage source, which may enhance particle trapping.

To study a higher current discharge would require a few modifications to the simulation code. Currently, the neutral gas is modeled as a constant background density. For larger currents, the depletion of the neutral species (due to ionization) would need to be tracked. This could be done using a 1D model in which each spatial cell tracks the average background density, which would be subjected to a nonlinear diffusion equation. At higher core densities, the Fokker-Planck model is more appropriate than the collisionless Vlasov equation. While this is much more computationally expensive, it could be selectively applied only to cells with a threshold particle density; this would mainly apply only to the central core region thereby reducing this computational cost.

ACKNOWLEDGMENTS

The authors thank W. Garrick (Research Computing, Portland State University) for help with the GPU computing server, as well as J. Solomon for the useful conversations regarding IEC fusion devices. We would also like to thank the New Energy Foundation (NEF) for financial assistance in this research.

APPENDIX: STEADY-STATE MODEL

In Ref. [21], Baxter and Stuart find analytic expressions for the phase space density of ions and fast neutral particles by using the method of characteristics to solve the steady-state Boltzmann equation. Inserting these expressions into the charge continuity equation results in the following expression [Eq. (11) in the reference]:

$$\begin{aligned} & \int_0^{\epsilon_0 x/l} d\epsilon \frac{l}{\epsilon_0} S\left(x - \frac{l\epsilon}{\epsilon_0}\right) - n_0 \int_0^x dx' \int_0^{\epsilon_0 x'/l} d\epsilon \\ & \times \sigma_{\text{ION}}(\epsilon) e^{-\xi(\epsilon)} \left[\epsilon \frac{l}{\epsilon_0} S\left(x' - \frac{l\epsilon}{\epsilon_0}\right) + n_0 \right. \\ & \left. \times \sigma_{\text{CX}}(\epsilon) \int_{l\epsilon/\epsilon_0}^{x'} dx'' \frac{l}{\epsilon_0} S\left(x'' - \frac{l\epsilon}{\epsilon_0}\right) \right] = \frac{mI_0}{e}. \end{aligned} \quad (\text{A1})$$

Here, ϵ represents energy, l is the interelectrode distance, ϵ_0 is the energy corresponding to the full cathode potential, x is the distance from the anode, σ_{ION} and σ_{CX} are the ionization and charge-exchange cross sections, $S(x)$ is an unknown spatially distributed ion source, and $\xi(\epsilon)$ is defined as

$$\xi(\epsilon) = \frac{n_0 l}{\epsilon_0} \int_0^\epsilon d\epsilon' \sigma_{\text{CX}}(\epsilon'). \quad (\text{A2})$$

Once the function $S(x)$ is determined, the ion and fast neutral density functions can be integrated to calculate the

fusion rate (see the reference for details). In the reproduction of this model, Eq. (A1) was integrated numerically to find $S(x)$. To do so, variable substitution was used to convert all integration to integration over x :

$$\begin{aligned} & \int_0^x dx' f\left[\frac{\epsilon_0}{l}(x-x')\right]S(x') \\ & - n_0 \int_0^x dx' \int_0^{x'} dx'' g\left[\frac{\epsilon_0}{l}(x'-x'')\right]S(x'') \\ & - n_0^2 \int_0^x dx' \int_0^{x'} dx'' h\left[\frac{\epsilon_0}{l}(x'-x'')\right] \\ & \times \int_0^{x''} dx''' Sx''' = \frac{mI_0}{e}, \end{aligned} \quad (\text{A3})$$

with the following definitions:

$$\begin{aligned} f(\epsilon) &= e^{-\xi(\epsilon)}, \quad g(\epsilon) = \sigma_{\text{ION}}(\epsilon)e^{-\xi(\epsilon)}, \\ h(\epsilon) &= \sigma_{\text{CX}}(\epsilon)\sigma_{\text{ION}}(\epsilon)e^{-\xi(\epsilon)}. \end{aligned} \quad (\text{A4})$$

On a uniform discrete grid, $S(x)$ is defined as $S(x) = S(n\Delta x)$. The $x = 0$ element is found by noting that $S(x)$ contains a Dirac delta term to describe the ion injection [this must be the case for Eq. (A3) to hold for any x]. The discrete representation of this 0th element is

$$S_0 = \frac{mI_0}{e\Delta x}. \quad (\text{A5})$$

For $x > 0$, both sides of Eq. (A3) can be differentiated, and written as a discrete sum (noting that $f(0) = 1$):

$$S_n - n_0 \sum_{i=0}^n \Delta x g_{n,i} S_i - n_0^2 \sum_{i=0}^n \Delta x h_{n,i} \sum_{j=0}^i \Delta x S_j = 0. \quad (\text{A6})$$

The coefficients $g_{n,i}$ and $h_{n,i}$ represent the functions $g(\epsilon_0/l(x_n - x_i))$ and $h(\epsilon_0/l(x_n - x_i))$, both of which go to 0 when $n = i$. Noting this, and picking off the last term of each

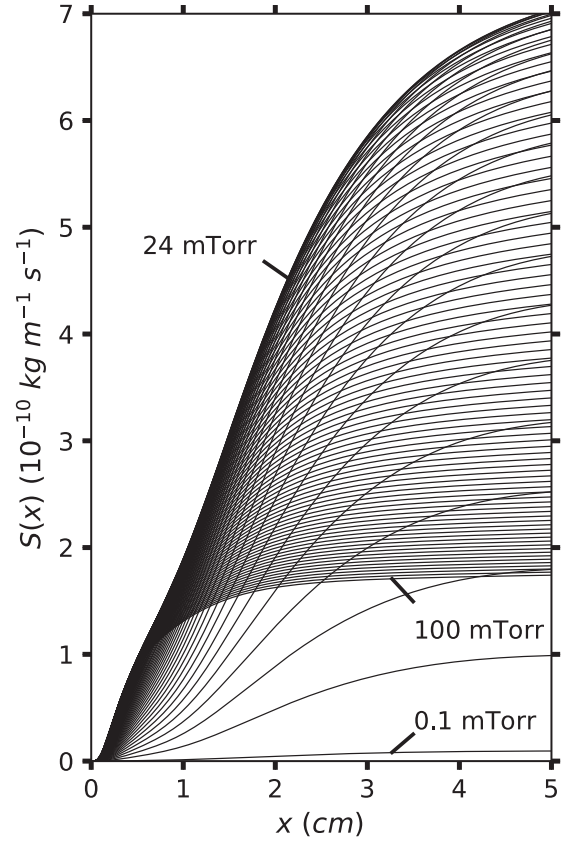


FIG. 12. The spatially distributed ion source function $S(x)$, as determined by Eq. (A7).

summation gives the following result:

$$S_n = n_0 \Delta x \sum_{i=0}^{n-1} \left(g_{n,i} S_i + n_0 \Delta x h_{n,i} \sum_{j=0}^i S_j \right). \quad (\text{A7})$$

Equation (A7) gives an iterative solution to the spatially distributed ion source, $S(x)$, which can then be used to evaluate the fusion rate. Examples of these source functions (excluding the Dirac delta term) are shown in FIG. 12.

[1] P. T. Farnsworth, Electric discharge device for producing interactions between nuclei, US Patent 3258402 (June 28, 1966).
 [2] R. L. Hirsch, Inertial-electrostatic confinement of ionized fusion gases, *J. Appl. Phys.* **38**, 4522 (1967).
 [3] P. T. Farnsworth, Method and apparatus for producing nuclear-fusion reactions, US Patent 3386883 (May 13, 1968).
 [4] T. H. Rider, A general critique of inertial-electrostatic confinement fusion systems, *Phys. Plasmas* **2**, 1853 (1995).
 [5] T. H. Rider, Fundamental limitations on plasma fusion systems not in thermodynamic equilibrium, *Phys. Plasmas* **4**, 1039 (1997).
 [6] W. M. Nevins, Can inertial electrostatic confinement work beyond the ion-ion collisional time scale? *Phys. Plasmas* **2**, 3804 (1995).
 [7] W. M. Nevins, A review of confinement requirements for advanced fuels, *J. Fusion Energy* **17**, 25 (1998).

[8] D. L. Bleuel, C. B. Yeaman, L. A. Bernstein, R. M. Bionta, J. A. Caggiano, D. T. Casey, G. W. Cooper, O. B. Drury, J. A. Frenje, C. A. Hagmann, R. Hatarik, J. P. Knauer, M. G. Johnson, K. M. Knittel, R. J. Leeper, J. M. McNaney, M. Moran, C. L. Ruiz, and D. H. G. Schneider, Neutron activation diagnostics at the national ignition facility (invited), *Rev. Sci. Instrum.* **83**, 10D313 (2012).
 [9] G. H. Miley, H. Momota, H. Leon, B. Ulmen, G. Amadio, A. Khan, G. Chen, W. Matisiak, A. Azeem, and P. Keutelian, Cylindrical IEC fusion neutron source for broad area NAA, *J. Eng. Gas Turb. Power* **133**, 124502 (2011).
 [10] J. C. Laul, Neutron activation analysis of geological materials, *At. Energy Rev.* **17**, 603 (1979).
 [11] B. B. Cipiti and G. L. Kulcinski, Embedded d-3he fusion reactions and medical isotope production in an inertial electrostatic confinement device, *Fusion Sci. Technol.* **44**, 534 (2003).

- [12] B. B. Cipiti, The fusion of advanced fuels to produce medical isotopes using inertial electrostatic confinement, Ph.D. thesis, University of Wisconsin, Madison, WI, 2004.
- [13] M. Strobl, I. Manke, N. Kardjilov, A. Hilger, M. Dawson, and J. Banhart, Advances in neutron radiography and tomography, *J. Phys. D* **42**, 243001 (2009).
- [14] N. Kardjilov, I. Manke, A. Hilger, M. Strobl, and J. Banhart, Neutron imaging in materials science, *Mater. Today* **14**, 248 (2011).
- [15] A. Buffler, Contraband detection with fast neutrons, *Radiat. Phys. Chem.* **71**, 853 (2004), 9th International Symposium on Radiation Physics (ISRP-9).
- [16] K. Yoshikawa, K. Masuda, T. Takamatsu, E. Hotta, K. Yamauchi, S. Shiroya, T. Misawa, Y. Takahashi, M. Ohnishi, and H. Osawa, Research and development on humanitarian landmine detection system by use of a compact d-d fusion neutron source, *Fusion Sci. Technol.* **52**, 1092 (2007).
- [17] N. Elsheikh, G. Viesti, I. ElAgib, and F. Habbani, On the use of a (252cf-3he) assembly for landmine detection by the neutron back-scattering method, *Appl. Radiat. Isot.* **70**, 643 (2012).
- [18] C. Dietrich, Improving particle confinement in inertial-electrostatic fusion for spacecraft power and propulsion, Ph.D. thesis, Massachusetts Institute of Technology, Cambridge, MA, 2007.
- [19] I. Radia and Y. Rep, Neutron Generators for Analytical Purposes, Radiation Technology Reports No. 1, IAEA, Vienna (2012).
- [20] B. J. Egle, Nuclear fusion of advanced fuels using converging focused ion beams, Ph.D. thesis, University of Wisconsin, Madison, WI, 2010.
- [21] D. C. Baxter and G. W. Stuart, The effect of charge exchange on ion guns and an application to inertial-electrostatic confinement devices, *J. Appl. Phys.* **53**, 4597 (1982).
- [22] F. Filbert, E. Sonnendrucker, and P. Bertrand, Conservative numerical schemes for the Vlasov equation, *J. Comput. Phys.* **172**, 166 (2001).
- [23] M. Ohnishi, Y. Yamamoto, M. Hasegawa, K. Yoshikawa, and G. H. Miley, Study on an inertial electrostatic confinement fusion as a portable neutron source, *Fusion Eng. Des.* **42**, 207 (1998).
- [24] K. Naborio, T. Sakai, and Y. Yamamoto, Investigation of spatial distribution of neutron production rate and its dependency on pressure in spherical IECF by one-dimensional simulations, in *20th IEEE/NPSS Symposium on Fusion Engineering* (IEEE, New York, 2003) pp. 59–71.
- [25] K. Naborio, Y. Yamamoto, Y. Ueno, and S. Konishi, Confinement of ions in an inertial electrostatic confinement fusion (iecf) device and its influence on neutron production rate, *Fusion Eng. Des.* **81**, 1701 (2005).
- [26] J. Büchner, Vlasov-code simulation, in *Advanced Methods for Space Simulation*, edited by H. Usui and Y. Omura (TERRA-PUB, Tokyo, JP, 2007), pp. 23–46.
- [27] H. S. Bosch and G. M. Hale, Improved formulas for fusion cross-sections and thermal reactivities, *Nucl. Fusion* **32**, 611 (1992).
- [28] R. Janev, D. Reiter, and U. Samm, *Collision Processes in Low-Temperature Hydrogen Plasmas* (Max Planck Institute for Plasma Physics, Jülich, DE, 2003).
- [29] M. A. Furman and M. T. F. Pivi, Probabilistic model for the simulation of secondary electron emission, *Phys. Rev. ST Accel. Beams* **5**, 124404 (2002).
- [30] E. J. Sternglass, Theory of secondary electron emission by high-speed ions, *Phys. Rev.* **108**, 1 (1957).
- [31] E. W. Thomas, International Atomic Energy Agency Report INDC(NDS)-322, Vienna, Austria (1995).
- [32] J. F. Ziegler, J. Biersack, and U. Littmark, *The Stopping of Ions in Matter* (Pergamon, New York, 1985).
- [33] J. F. Ziegler, M. D. Ziegler, and J. P. Biersack, Srim - the stopping and range of ions in matter (2010), *Nucl. Instrum. Meth. B* **268**, 1818 (2010).
- [34] S. Y. Lai, D. Briggs, A. Brown, and J. C. Vickerman, The relationship between electron and ion induced secondary electron imaging: A review with new experimental observations, *Surf. Interface Anal.* **8**, 93 (1986).
- [35] T. A. Thorson, R. D. Durst, R. J. Fonck, and A. C. Sontag, Fusion reactivity characterization of a spherically convergent ion focus, *Nucl. Fusion* **38**, 495 (1998).
- [36] K. L. Wilson and A. E. Pontau, The temperature dependence of deuterium trapping in fusion reactor materials, *J. Nucl. Mater.* **85-86**, 989 (1979).
- [37] S. M. Myers, S. T. Picraux, and R. E. Stoltz, Defect trapping of ion-implanted deuterium in fe, *J. Appl. Phys.* **50**, 5710 (1979).
- [38] R. A. Langley, J. Bohdansky, W. Eckstein, P. Mioduszewski, J. Roth, E. Taglauer, E. W. Thomas, H. Verbeek, and K. L. Wilson, Data compendium for plasma-surface interactions, *Nucl. Fusion* **24**, S9 (1984).
- [39] R. Bowden-Reid, J. Khachan, J.-P. Wulfkühler, and M. Tajmar, Evidence for surface fusion in inertial electrostatic confinement devices, *Phys. Plasmas* **25**, 112702 (2018).
- [40] J. Kasagi, H. Yuki, T. Baba, T. Noda, T. Ohtsuki, and A. G. Lipson, Evidence for surface fusion in inertial electrostatic confinement devices, *J. Phys. Soc. Jpn.* **71**, 2881 (2002).
- [41] M. Bakr, K. Masuda, and M. Yoshida, Improvement of the neutron production rate of iec fusion device by the fusion reaction on the inner surface of the iec chamber, *Fusion Sci. Technol.* **75**, 479 (2019).
- [42] R. A. Nebel and D. C. Barnes, The periodically oscillating plasma sphere, *Fusion Technol.* **38**, 28 (1998).
- [43] J. Park, R. A. Nebel, S. Stange, and S. K. Murali, Periodically oscillating plasma sphere, *Phys. Plasmas* **12** 056315-1 (2005).